International Journal of Climatology

International Journal of Climatology RMetS

RESEARCH ARTICLE OPEN ACCESS

Synchronisation of Extreme Precipitation and Sea Surface Temperature Events in the Northern Hemisphere: A Complex Network Approach

Connor Saari[1] | Jürgen Kurths[2,3] | Gabriele Villarini[4,5] | Behzad Ghanbarian[6,7,8]

[1]Porous Media Research Lab, Department of Geology, Kansas State University, Manhattan, Kansas, USA | [2]Potsdam Institute for Climate Impact Research, Potsdam, Germany | [3]Department of Physics, Humboldt University of Berlin, Berlin, Germany | [4]Department of Civil and Environmental Engineering, Princeton University, Princeton, New Jersey, USA | [5]High Meadows Environmental Institute, Princeton University, Princeton, New Jersey, USA | [6]iResearchE^3 Lab, Department of Earth and Environmental Sciences, University of Texas at Arlington, Arlington, Texas, USA | [7]Department of Civil Engineering, University of Texas at Arlington, Arlington, Texas, USA | [8]Division of Data Science, College of Science, University of Texas at Arlington, Arlington, Texas, USA

Correspondence: Behzad Ghanbarian (ghanbarianb@uta.edu)

Received: 5 August 2025 | **Revised:** 14 November 2025 | **Accepted:** 25 November 2025

Keywords: complex networks | extreme events | network science | precipitation | sea surface temperature | synchronisation | teleconnections

ABSTRACT

Synchronisation, the tendency of climatic events to occur simultaneously, can arise from small-scale and large-scale atmospheric dynamics. Climate variables can be synchronised across broad spatial and temporal scales, manifesting as regional, continental and global teleconnection patterns. In the study, we analysed spatiotemporal patterns of inland extreme precipitation events (EPEs) and extreme sea surface temperature events (ESSTEs) in the Northern Hemisphere (0°N–60°N) to better understand their connection. Using gridded monthly gauge- and interpolation-based datasets for precipitation and sea surface temperature from 1930 through 2020, we detected extreme events based on the 95th percentile threshold. We then quantified the synchronisation between extreme events using the event synchronisation (ES) method and compared our findings to a null model distribution to ensure that the identified links were non-random. Subsequently, we constructed EPE and ESSTE complex networks and calculated key network metrics including degree centrality (k), mean geographic distance (MGD) and clustering coefficient (C). Our results showed that the EPEs and ESSTEs exhibited non-monotonic trends over the past nine decades, with significant increasing trends after 1980. Key EPE network hubs were detected in Mexico, the African Sahel and parts of Asia, while ESSTE hubs appeared in the Atlantic Ocean near the UK and US borders, the Pacific Ocean close to East Asia and the Mediterranean and Red Seas. Analyses of MGD and C revealed that the EPE network had larger MGDs and more intense local clustering in continental areas (Sahel and East Asia), indicating that EPEs experience teleconnections within these locations even though they also experience strong local associations. The findings of our EPE network contrast with those of our ESSTE network, which had lower MGD values and close clustering within specific ocean basins, as expected due to localised ocean–atmosphere coupling. Our findings suggest that the drivers for extreme climate events are complex and can lead to strong local and global connections.

1 | Introduction

Extreme precipitation events (EPEs) in the Northern Hemisphere are influenced by various climatic and atmospheric processes, among which tropical cyclones play a critical role. Dare and McBride (2011) reported that 98.3% of tropical cyclones formed over sea surface temperatures (SSTs) above 25.5°C, emphasising the importance of oceanic warming in cyclone development. Rising SSTs enhance atmospheric moisture through intensified evaporation, amplifying extreme precipitation globally (Alexander et al. 2009; van der Ent and Savenije 2013; O'Gorman 2015). As tropical cyclone activity intensifies in a warming climate (Walsh et al. 2015; Knutson et al. 2020), extreme weather events are expected to become more frequent and severe (Kotz et al. 2022; Kunze 2021). Understanding the spatiotemporal behaviour of these extremes is therefore of great importance.

Extreme precipitation exhibits strong spatial and temporal variability (Boers et al. 2019; Oladoja et al. 2025), which is further intensified by anthropogenic warming (Trenberth 2011; Marvel and Bonfils 2013). Numerous studies have demonstrated positive relationships between SST and precipitation, as the atmosphere's capacity to retain moisture increases with temperature (Roxy 2013; Trenberth and Shea 2005; Fowler et al. 2021). The IPCC (2023) AR6 highlights that global warming has likely increased both the frequency and intensity of EPEs since the mid-20th century. Regional studies have reported similar trends, such as intensifying monsoon extremes in South Asia (Falga and Wang 2022) and strong SST–precipitation coupling over tropical regions of the Northern Hemisphere (Ekhtiari et al. 2021).

SST variability strongly modulates global precipitation. For instance, El Niño- and La Niña-related SST anomalies affect rainfall and river discharge in regions such as Florida (Sun and Furbish 1997) and South Texas (Murgulet et al. 2017), suggesting that SST anomalies can act as precursors to EPEs. Numerous studies have explored SST–precipitation relationships (Ting and Wang 1997; Alexander et al. 2009; He et al. 2018; Yang and Huang 2023), showing that SST patterns, particularly in the Pacific, can influence continental rainfall and monsoon systems (Singh 2001; Barros and Silvestri 2002). Using moisture tracking algorithms, van der Ent and Savenije (2013) quantified ocean-to-land moisture transport, confirming the critical role of SST in modulating inland precipitation. In another study, Hatsuzuka and Sato (2022) investigated the effect of SST on EPEs in North Japan using large-ensemble simulations and showed that in years with higher SSTs over the Sea of Japan, the increased atmospheric moisture could increase the extreme precipitation in the inland area of Hokkaido, depending on weather patterns. In another study, Kang et al. (2021) analysed an EPE in Korea that occurred on 13 August 13 2012, with 430 mm in less than 12 h causing destructive landslides and devastating flash floods. They noticed that the SST over the Yellow Sea was unusually 1 °C higher than the 30-year average during that EPE. In another study, Dong et al. (2018) addressed the role of SST on extreme precipitation on the US West Coast during the winter season (December–February). They found that Pacific SST patterns could explain about 20% of the variance in West Coast extreme precipitation, often tied to atmospheric rivers (ARs), narrow corridors of intense water vapour transport.

Recent analyses (e.g., Kumar et al. 2013; He et al. 2018) demonstrate that SST–precipitation correlations are typically stronger over oceans than land, where complex topography and land–atmosphere feedbacks weaken linear relationships. Tropical monsoon rainfall, for example, is particularly sensitive to local SST anomalies (Roxy 2013). Observational records further indicate upward trends in precipitation and SSTs: land precipitation in the Northern Hemisphere has increased by 1.2%–1.8% per decade since the 1950s (IPCC SR15), while global extra-polar SSTs have warmed by about 0.20°C per decade (Lindsey and Dahlman 2025). These trends have contributed to a growing frequency of EPEs worldwide (Groisman et al. 2005; Rummukainen 2012).

Traditional statistical approaches, such as empirical orthogonal function (EOF) analysis, have been widely used to examine spatiotemporal variations in climatic variables (Hannachi et al. 2009), but they often struggle to capture nonlinear and propagating features. In contrast, complex network theory provides an effective framework to analyse large-scale climate systems and their teleconnections (Boers et al. 2014; Ludescher et al. 2021; Fan et al. 2021). Network-based analyses have uncovered major climate patterns, including El Niño/Southern Oscillation (ENSO), Pacific Decadal Oscillation (PDO) and Indian Ocean Dipole (IOD), as well as long-range teleconnections that are not easily detectable by correlation or EOF methods (Agarwal et al. 2019; Boers et al. 2019). These studies demonstrate the potential of complex networks for identifying synchronisation, propagation and predictability in climate systems. For example, Ludescher et al. (2021) successfully applied complex network analysis to forecast events such as El Niño episodes, Amazon droughts and Indian monsoon extremes.

Despite recent advances, many aspects of ocean–atmosphere coupling, particularly those involving extreme SST variations and their influence on precipitation extremes, remain poorly understood. Ekhtiari et al. (2019, 2021) analysed coupled SST–precipitation networks at the global scale, but their focus included all events rather than extremes, and their datasets were limited in spatial and temporal resolution. Similarly, although numerous studies have independently investigated SST (Novi et al. 2021; Zhao et al. 2023) and precipitation (Boers et al. 2019; Gupta et al. 2022) networks, most prior SST-related research has emphasised all events (e.g., Ekhtiari et al. 2019, 2021) rather than extremes and has often relied on lower-resolution datasets and shorter temporal coverage. Moreover, spatiotemporal analysis of extreme SSTs using complex network theory has been very limited, with Benedetti-Cecchi (2021) examining marine heatwaves using daily SST data and network theory to identify synchronisation and tipping points, but considering only SST. Together, these gaps underscore the need to explore extreme SST and precipitation events jointly.

Understanding the spatiotemporal relationships between EPEs and extreme sea surface temperature events (ESSTEs) is crucial because extremes in oceanic and atmospheric systems are often interlinked through large-scale teleconnection patterns. Identifying these relationships can improve our understanding of how extreme SST anomalies influence or synchronise with extreme precipitation across regions, thereby offering insights into the mechanisms driving compound and cascading climatic hazards. Building on this motivation, the main objectives of this study are to: (1) uncover spatiotemporal relationships of EPEs and ESSTEs; (2) demonstrate the capability of complex network theory to identify synchronisation structures; and (3) integrate our findings into a broader climatological framework, particularly in the context of atmospheric teleconnections and hubs.

2 | Materials and Methods

2.1 | Data

The monthly SST data used in this study were collected from Berkeley Earth's Global Gridded Temperature database, which consists of approximately 16,000 grids (known as nodes within complex network theory) globally, with a resolution of 1°×1° and a temporal range of 1850–2020. The monthly precipitation data were collected from the Global Precipitation Climatology Center (GPCC) database and include data from 1891 to 2020 with a 1°×1° resolution. These two databases were selected because they share overlapping time frames, spatial resolution (1°×1°) and monthly reporting frequency. Our pre-processing analyses showed large amounts of either incomplete or unreliable data in the interpolated monthly precipitation data before 1930. Certain data were missing for multiple years, or repeated interpolated data that were shared from node to node over large spatiotemporal extents. Thus, the data were trimmed to the years 1930 through 2020, which time span held more reliable data. After pre-processing, we ended with 8516 and 13,083 grid points for the precipitation and SST networks, respectively, in the Northern Hemisphere.

Flooding in coastal areas in the United States and China occurs during the hurricane/typhoon season. Based on NOAA's Tropical Cyclone Climatology report (https://www.nhc.noaa.gov/climo/), most hurricanes in the Northern Hemisphere happen from June to November. Paprotny et al. (2018) analysed flood events that occurred across Europe between 1870 and 2016 using the HANZE database, which includes records of flash, river and coastal floods (see their fig. 2). In southern Europe, flash floods were the dominant flood events, with peak occurrences observed between September and November. In contrast, central and western Europe experienced a higher frequency of river floods compared to flash floods, with associated flood losses predominantly concentrated between June and August. We, therefore, analysed the precipitation and SST data from June to November (hereafter JJASON) and restricted our data analysis to this 6-month period.

2.2 | Extreme Precipitation and SST Events

There are various methods, such as extreme value theory (Buishand 1989), to identify extreme events in time series. However, for the sake of simplicity, we applied the threshold approach. More specifically, we assumed that precipitation and SST events with values above the 95th percentile for all months were extremes at each node. Using the 95th percentile threshold, we constructed the extreme precipitation and SST events (EPEs and ESSTEs) series composed of zeros and ones representing non-extreme and extreme events, respectively. This is because our focus was on the number of extreme events and their synchronisations, not their magnitudes.

2.3 | Complex Network Theory

We constructed climate networks in which nodes represented geographic locations (or grid points) and were connected to each other via links (also known as edges). In the following sections, we explain how the similarities between any two extreme event series were determined and how the similarity and adjacency matrices were created.

2.3.1 | Event Synchronisation (ES)

To calculate the level of similarity between two extreme event series and measure the synchronisation of extreme events between the nodes, we used the ES method (Quiroga et al. 2002). The degree of similarity between any pair of grid points was computed by counting the number of synchronised events for each pair and using the time delay $\Delta^{i,j}_{m,n}$ that meets the condition of $\left|\Delta^{i,j}_{m,n}\right| < \tau^{i,j}_{m,n}$ and $\left|\Delta^{i,j}_{m,n}\right| \leq \tau_{\max}$. $\Delta^{i,j}_{m,n}$ and $\tau^{i,j}_{m,n}$ are defined as

$$\Delta^{i,j}_{m,n} = t^{j}_{n} - t^{i}_{m} \tag{1}$$

$$\tau^{i,j}_{m,n} = \frac{1}{2} \times \min\left\{\Delta^{i,i}_{m,m-1}, \Delta^{i,i}_{m,m+1}, \Delta^{j,j}_{n,n-1}, \Delta^{j,j}_{n,n+1}\right\} \tag{2}$$

where $\tau^{i,j}_{m,n}$ is the local time scale, which may change depending on extreme events. Within the ES method, $\tau_{\max}$ constrains $\Delta^{i,j}_{m,n}$ to maintain realistic synchronisation between events (Boers et al. 2014). We set $\tau_{\max} = 0$ to analyse the EPEs and ESSTEs occurring within the same month in the Northern Hemisphere. Using the ES values, the similarity matrix containing the degree of synchronisation among the nodes was then created.

Equations (1) and (2) are general formulations that define the ES metric and are not dependent on the temporal resolution of the data. Whether the input data are at daily or monthly resolution, these equations remain valid, as they describe the synchronisation between events irrespective of the specific time step used.

2.3.2 | Adjacency Matrix

To establish statistically meaningful links among the nodes and accurately compute the adjacency matrix composed of zeros (no links) and ones (representing links), we used a null-model distribution. To minimise the bias associated with random links, we shuffled each extreme event series 1000 times and then calculated the ES value via the ES method. Next, the distribution of the calculated ES values was analysed at each node. For this purpose, we determined the 99.5th percentile threshold for each pair of nodes and computed the corresponding ES value, that is, ES^{ij}_{thresh}. If the ES value determined based on the original (unshuffled) extreme event series was greater than the ES^{ij}_{thresh}, then a link was established between those two nodes and the corresponding element in the adjacency matrix was set equal to one. This approach was used to maintain quality control and establish only connections not caused by coincidence or by inherent biases caused by event rate differences in the nodes time series.

2.4 | Network Measures

In this section, we briefly describe several network measures, that is, degree centrality (k), mean geographical distance (MGD) and clustering coefficient (C), commonly used in the complex network literature (Donges et al. 2009; Jamali et al. 2023;

Feldhoff et al. 2014), and explain how we use them to analyse the spatiotemporal patterns of the EPEs and ESSTEs.

2.4.1 | Degree

The degree of node i (k_i) represents the number of connections that it has with other nodes. In other words, k_i indicates the magnitude of connectivity. This metric measures the importance of a node within the network structure. Specifically, in our context, it reflects the level of association between extreme events occurring at a particular node and those at other nodes. To gain insights into the propagation dynamics within the constructed networks, we calculated k_i as follows:

$$k_i = \sum_{j=1}^{N} A_{(i,j)} \tag{3}$$

where N represents the total number of nodes in the network. In Equation (3), $A_{(i,j)}$ denotes an entry of the adjacency matrix—equal to 1 if nodes i and j are connected (i.e., their extreme events are synchronised), and 0 otherwise—such that the sum is a count of how many significant associations node i has. Nodes with high degrees are called hubs. In climate networks, nodes with high degrees represent important locations for propagation or teleconnection.

2.4.2 | MGD

The MGD quantifies the average spatial separation between a node and its connected neighbours. This metric assesses whether a node's extreme patterns are more closely aligned with nearby regions or with distant areas. A higher MGD suggests that the node is involved in teleconnections, long-distance climate interactions, while a lower MGD indicates influence confined to local geographic regions. The MGD is given by

$$MGD_i = \frac{1}{k_i} \sum_{j=1}^{n} D_{(i,j)} A_{(i,j)} \tag{4}$$

where $D_{(i,j)}$ is the geographic distance between nodes i and j and $A_{(i,j)}$ denotes the set of neighbours of node i. We used the MGD, along with our other network measures, to determine the localities of influence among the nodes.

2.4.3 | Clustering Coefficient

The clustering coefficient (C_i) provides insights into the extent to which neighbours of a specific node are interconnected, offering a measure of local link density. It measures how many nodes that share links with a specified node are connected. The value of C_i is determined as follows:

$$C_i = \frac{2L_i}{k_i\left(k_i - 1\right)} \tag{5}$$

where L_i is the number of links among k neighbours of node i. The C_i ranges between 0, indicating no connections among the neighbours of node i, and 1, signifying that all neighbours of node i are interconnected. C_i may be used as a measure of spatial coherency for the occurrence of our ESSTEs and EPEs. C_i values approaching 0 in a location are interpreted as having low spatial coherency, meaning any event which occurs at a given node would likely not have a significant effect on the surrounding nodes. Conversely, a high C_i approaching the value of 1 is interpreted as having a high degree of spatial coherency and means that local events are likely to have some influence on connected nodes.

2.5 | Spatial Boundary Effect

At spatial scales smaller than the global (e.g., national, continental or semi-global), the accuracy of climate networks can be affected by boundary limitations. Nodes located near the edges of the study domain may have potential physical or climatic connections with nodes outside the defined boundary; however, such connections are not captured in the network due to the imposed spatial limits of the study area. For example, in our analysis, nodes situated near the equator could have real-world connections to nodes in the Southern Hemisphere, but these cross-boundary links are excluded, which may bias the characterisation of our ESSTE and EPE networks. To minimise such boundary effects, we applied a surrogate-based method proposed and successfully evaluated by Rheinwalt et al. (2012). This approach involves correcting network measures by normalising each node's value against the expected value obtained from surrogate networks. In this context, surrogate networks are randomised versions of the original network that preserve its overall structure (e.g., the number of nodes and links) but randomise the associated values or weights.

We generated an ensemble of 1000 surrogate networks by maintaining the original network topology while shuffling its values. For each grid point i, we then calculated the arithmetic mean of each network measure across the ensemble, denoted as $\left\langle M_i^{sur} \right\rangle$. The corrected measure was then obtained by subtracting this surrogate average from the original value, that is, as follows:

$M_i^{cor} = M_i - \left\langle M_i^{sur} \right\rangle$. Finally, to enable consistent comparison across all grid points, the corrected measures were rescaled using min–max normalisation to map their values onto the interval [0,1]. This procedure effectively reduces biases associated with boundary effects and provides a more accurate representation of node-level dynamics within the network.

3 | Results and Discussion

In this section, we present the results of the synchronisation of EPEs and ESSTEs in the Northern Hemisphere. We also discuss the mechanisms that drive continental and global-scale synchronisation among EPEs and ESSTEs.

3.1 | Precipitation and SST Data Analyses

The spatial distribution of the average monthly precipitation and SST as well as their 95th percentiles are shown in Figure 1 for the JJASON. As shown in Figure 1a,b, in general, the results

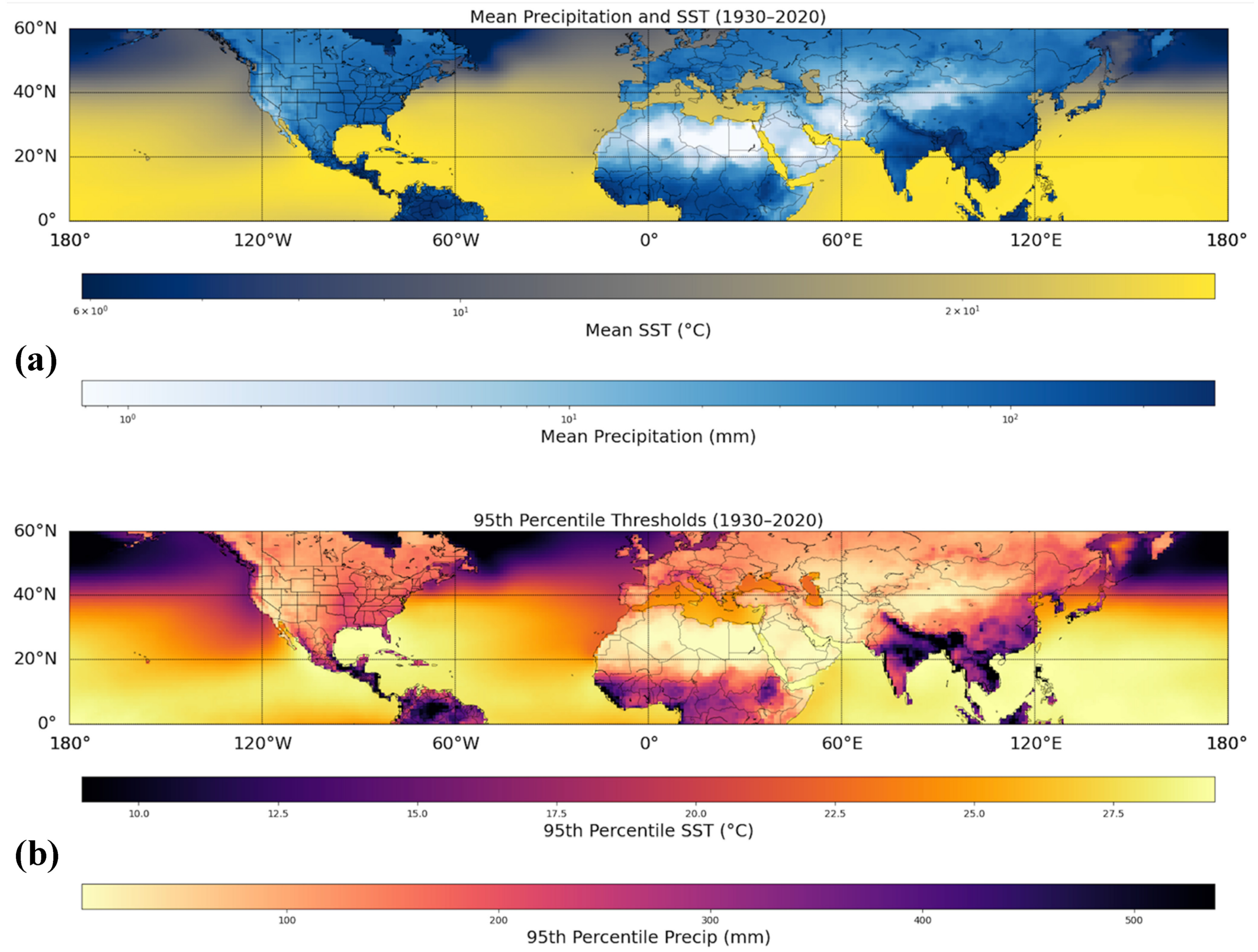

FIGURE 1 | (a) Average monthly precipitation and SST (top) and (b) the 95th percentile for precipitation and SST (bottom) within the Northern Hemisphere for the data from 1930 to 2020. [Colour figure can be viewed at wileyonlinelibrary.com]

are consistent with previous studies that reported similarities between mean and 95th percentile maps for various climate networks (Jamali et al. 2023; Oladoja et al. 2025; Bosikun et al. 2025). Figure 1b shows regions with the highest thresholds for the SST (i.e., 95th percentiles exceeding 27.5°C) including the Gulf of Mexico, the western Atlantic Ocean adjacent to the US southeast, the Red Sea, Gulf of Aden, Persian Gulf, Gulf of Oman, Bay of Bengal South China Sea and the Philippine Sea in the western Pacific Ocean near southeastern China. These regions correspond to common pathways of tropical cyclones and hurricanes in the Northern Hemisphere, generally occurring between 5°N and 30°N, as reported by the National Hurricane Center (https://www.nhc.noaa.gov/climo/). More specifically, Atlantic hurricanes predominantly develop and propagate across the Atlantic Ocean, the Caribbean Sea and the Gulf of Mexico (Garner et al. 2021).

Regions with 95th percentiles exceeding 27.5°C (Figure 1b) satisfy the minimum requirement for tropical cyclone formation. Dare and McBride (2011) collected 6-hourly data from the National Oceanic and Atmospheric Administration/National Climatic Data Center (NOAA/NCDC) SST dataset and analysed all tropical cyclone formations within 35° latitude of the equator during the period 1981–2008. Their results showed that 98.3% of tropical cyclones formed at SST values exceeding 25.5°C, indicating a robust empirical threshold for cyclone genesis. They also found that this temperature threshold was not sensitive to the specific maximum wind speed criterion used to define formation. However, it is notably influenced by short-term SST fluctuations occurring during the development phase.

Figure 1b also presents the spatial distribution of the 95th percentile of monthly precipitation. Regions exhibiting the highest thresholds (exceeding 450 mm) include southern and southeastern US, southern Mexico, northern portions of South America and several West African countries, that is, Senegal, Gambia, Guinea, Sierra Leone, Liberia and Nigeria. In Asia, areas with similarly high precipitation thresholds encompass the Himalayan region, eastern India, Bangladesh, Vietnam and northern Malaysia. The exceptionally high monthly precipitation thresholds in these regions are strongly associated with the timing and dynamics of seasonal monsoons (Kane 1999; Malik et al. 2010; Boers et al. 2013; Cui et al. 2019; Strnad et al. 2025) as well as tropical cyclones and hurricanes (Terry and Kim 2015; Mullens 2021).

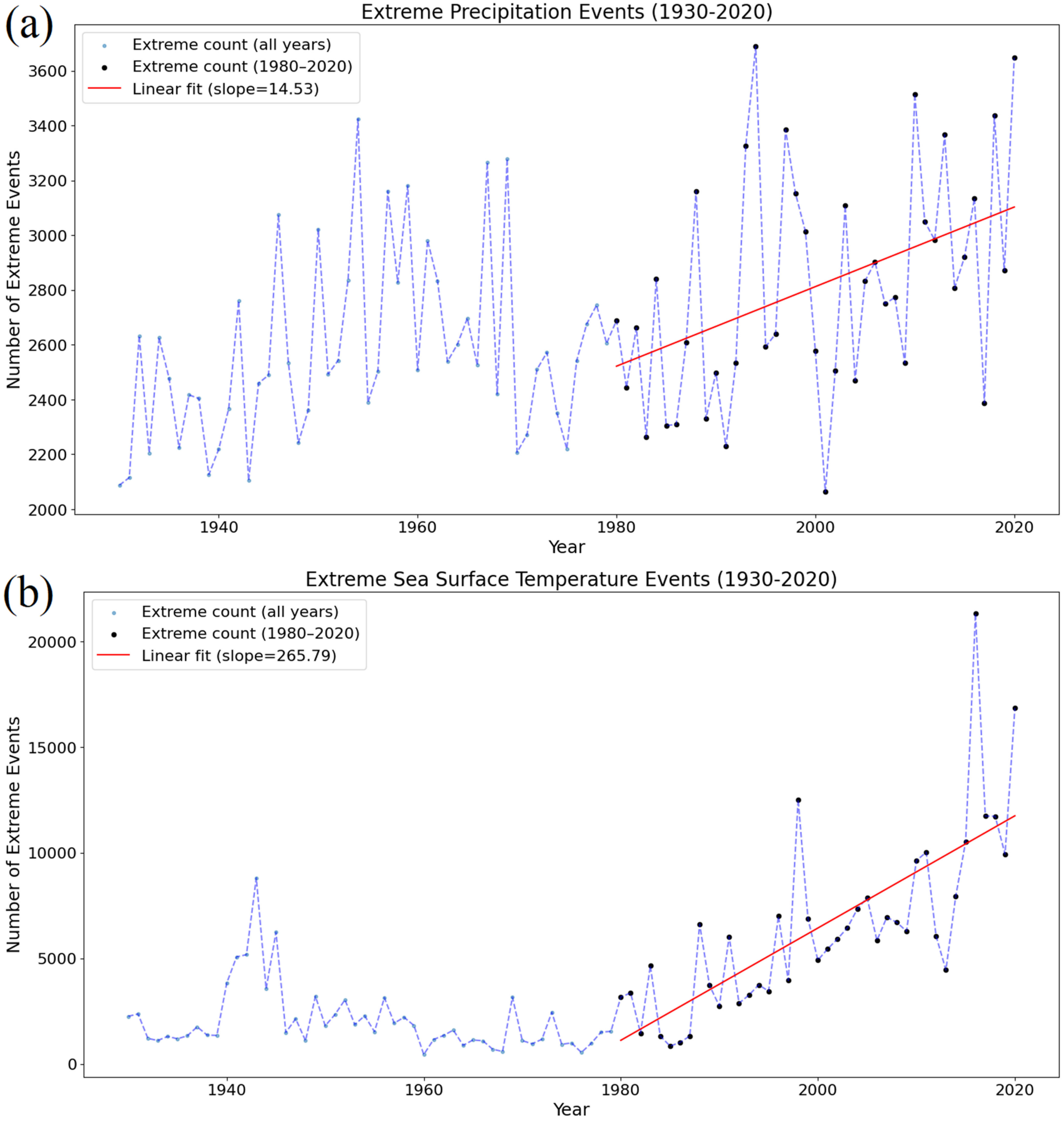

FIGURE 2 | (a) Number of EPEs (top) and (b) number of ESSTEs (bottom) as a function of year. The red solid line represents the fit of the linear model to the data from 1980 to 2020. The dashed blue lines are for the sake of visibility of yearly changes. [Colour figure can be viewed at wileyonlinelibrary.com]

3.2 | Temporal and Spatial Trends in Extreme Events

To analyse the overall temporal trend in the number of extreme events in the Northern Hemisphere, we first plotted the number of extreme events versus the year and performed some regression analyses to detect the trends in the EPEs and ESSTEs. For this purpose, we included all data from all nodes. The overall trend in the data is nonlinear and nonmonotonic, as shown in Figure 2. Due to significant scatter and fluctuations in the data, we restricted the linear fit to the period 1980–2020, during which a more pronounced increasing trend in the number of EPEs and ESSTEs is observed (Figure 2). Using ordinary least squares with a p value < 0.05, we found statistically significant slopes of 14.53 and 265.79 for the EPEs and ESSTEs, respectively.

Results presented in Figure 2a are consistent with those of Alexander (2016), who reported an increase in the proportion of land area in the Northern Hemisphere experiencing a rising

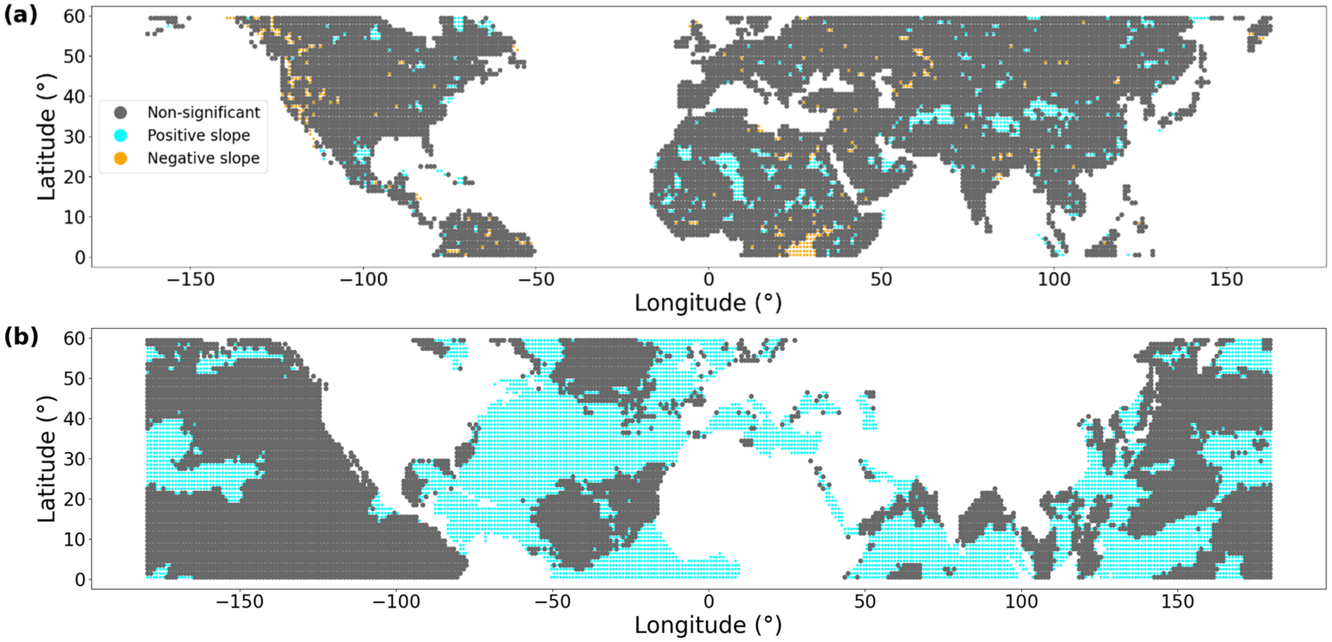

FIGURE 3 | Node-based trends in the (a) EPEs and (b) ESSTEs within the study area of 0°N–60°N and using the linear trend for the years 1980–2020. Blue dots represent a statistically significant increase in trend, while the orange dots denote the opposite. Grey dots represent no significant change. [Colour figure can be viewed at wileyonlinelibrary.com]

percentage of EPEs. Our ESSTE results (Figure 2b) align with recent findings from the Copernicus Climate Change Service (Copernicus Climate Change Service 2023), which reported record-breaking SST anomalies in the North Atlantic that have contributed to extreme marine heatwaves in recent years. These increasing ESSTEs reflect broader trends of rising ocean temperatures, which may influence the frequency and intensity of EPEs. We should also note that the trend of global mean surface temperature was not monotonic in the 20th century: it increased from the early 1900s to the 1940s, declined slightly during the mid-century, and then rose sharply from the mid-1970s onward (Thompson et al. 2010).

To detect which regions in the Northern Hemisphere have been significantly impacted by extreme events over time, we further analysed the number of extreme events at each node and their trends via linear regression. For this purpose, we plotted the number of extreme events against the year, fit a linear regression to the data from 1980 to 2020 at each node and then investigated whether the slope was significantly positive or negative at the 5% significance level.

Results for the EPEs are presented in Figure 3a in which nodes with statistically significant positive slopes are shown via the blue dots, while those with statistically significant negative slopes are shown via the orange dots. The black dots represent the nodes with statistically non-significant (zero) slopes. Blue dots in Figure 3a refer to some regions in Russia, western China, Pakistan, Afghanistan, Saudi Arabia, Iran, Turkey and in Asia, Niger, Mali, Ethiopia and Somalia in Africa, Ukraine and Spain in Europe, Mexico, Texas (USA) and North and North East of Canada in North America. The results of our statistical analysis shown in Figure 3a are consistent with some recent severe floods around the world, such as Pakistan (Shehzad 2023), Texas (Green et al. 2025) and western China (Wang et al. 2025). For instance, Zittis et al. (2022) argued that extreme precipitation and flood events in the Middle East are because greenhouse gas emissions in this region are rising rapidly and exceeding those of the European Union. They noticed that the region has experienced accelerated warming compared to other inhabited areas, particularly in recent decades, with an average increase of approximately 0.45°C per decade. Additionally, evident shifts in the hydrological cycle and increasing occurrences of extreme weather events pose major societal challenges, including more intense rainfall events capable of triggering flash floods (Zittis et al. 2022).

As shown in Figure 3b, numerous regions in the seas and oceans in the Northern Hemisphere have significantly positive increasing trends in the number of ESSTEs, particularly in the Pacific Ocean, Indian Ocean and Atlantic Ocean. Our results are in accord with those reported by Merchant et al. (2025), who found that the global mean SST increased from 0.06 K per decade during 1985–1989 to 0.27 K per decade between 2019 and 2023, which indicates a more than fourfold acceleration in ocean warming.

There is strong evidence showing that across various temporal scales extreme SST anomalies in the oceans can trigger extreme inland precipitation events through mechanisms involving moisture transport, teleconnections, and altered atmospheric circulation. Various studies show that Atlantic SST anomalies are one of the most important mechanisms for precipitation and extreme precipitation in Eurasia (Bothe et al. 2011; Zhang et al. 2020).

3.3 | Network Measures

In the following sections, we present the results of complex network theory and more specifically, network measures obtained

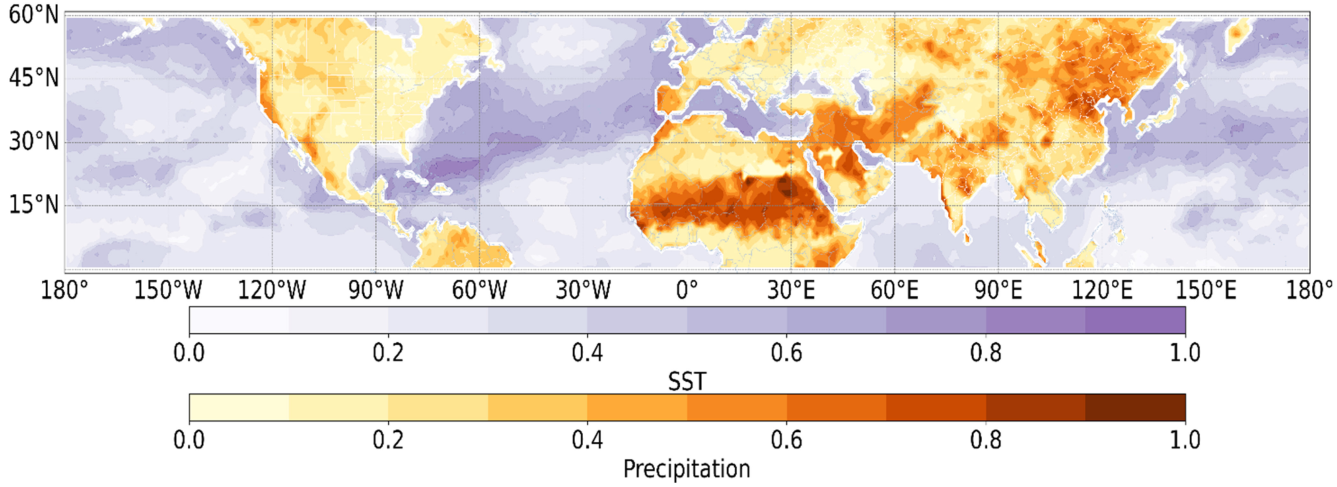

FIGURE 4 | Degree values, corrected for spatial boundary effects, within the Northern Hemisphere (0°N–60°N) for data from 1930 to 2020. Results for the EPEs are shown with warm tones (bottom colour bar), while for the ESSTEs with cool tones (top colour bar). The numerical scale is the same for both, ranging from 0 to 1. [Colour figure can be viewed at wileyonlinelibrary.com]

by analysing the EPEs and ESSTEs within the Northern Hemisphere during the defined months of JJASON. Recall that all network measures were adjusted to account for spatial boundary effects, subsequently normalised and rescaled to the interval [0,1]. Moreover, $\tau_{\max}$ was set to 0, implying that the analysis focused exclusively on extreme events occurring synchronously within the same month. Therefore, those synchronous events that happened at greater time scales (i.e., more than a month) were not analysed in this study.

3.3.1 | Degree

The quantity k is a fundamental measure that quantifies the importance of a node based on the number of its direct connections to other nodes in a network. A node with high degree has many direct connections (known as hub or super node), while a node with low degree has few connections and therefore is isolated.

Figure 4 presents the degree values for both the EPE and ESSTE networks constructed using $\tau_{\max} = 0$. As can be seen, high degree values are observed in both networks. Recall that regions with high degrees (known as hubs) indicate locations where EPEs or ESSTEs occur synchronously with many other locations.

Hubs within the EPE network include northwestern Mexico, US West Coast, the southwestern coast of India, central to eastern China and Mongolia, as well as some regions in southeastern Russia and northern Kazakhstan. We also observed high k values in the African Sahel, a semiarid region extending from the Atlantic Ocean to the Red Sea, encompassing countries such as Senegal, Mali, Niger, Chad and Sudan. This region, acting as a transitional zone between the Sahara Desert and more fertile savannas, is characterised by a harsh climate with seasonal rainfall and sparse vegetation. The Sahel is remarkably dry and arid, where minimal precipitation is evenly distributed across vast continental areas with rare small-scale extreme events. The low precipitation gradient here leads to high connectivity across large spatial scales. Hubs detected in the Sahel (Figure 4) are consistent with those reported by Scarsoglio et al. (2013), who used monthly precipitation data from 1941 to 2020 in the GPCC database. More specifically, they constructed the complex network using the precipitation data (not extreme values) and reported high degrees in Sahel, eastern Australia and northern Europe (see their fig. 2).

The African Sahel is close to the equator, the lower boundary in our study. Our results, however, are consistent with those of Scarsoglio et al. (2013) who analysed the precipitation data at the global scale. This clearly shows that the spatial boundary effects were minimised in our study. This means that the approach developed by Rheinwalt et al. (2012) was effective and accurate for our case.

Figure 4 also shows the hubs in the ESSTEs network detected in the Atlantic and Pacific Oceans between 30°N and 60°N. More specifically, we observed hubs off the eastern coast of the United States, surrounding the United Kingdom, in the Baltic Sea, in the Mediterranean and Red Seas, the Sea of Japan, the East China Sea and the Sea of Okhotsk. Climatologically, the high k values in regions like northwestern Mexico, the southwestern coast of India, north-northeastern China and Mongolia likely result from orographic effects and monsoonal dynamics. Orography enhances localised convection and, together with large-scale atmospheric flows, modulates teleconnections (Adam et al. 2006; Shige and Kummerow 2016). In Africa, the extensive band of high k values suggests that the African Easterly Jet and associated regional teleconnections (e.g., ENSO and IOD) are key drivers of synchronous precipitation extremes (Nicholson 2013). Along the eastern coast of the United States, the United Kingdom and adjacent seas, high k hubs coincide with major oceanic boundary current systems such as the Gulf Stream and Kuroshio Current, which anchor persistent SST anomalies and influence teleconnections (Deser et al. 2010; NOAA Climate.gov).

Mondal et al. (2020) and Jamali et al. (2023) analysed daily precipitation data, constructed EPE networks and reported hubs in the northeastern and northern parts of the CONUS for

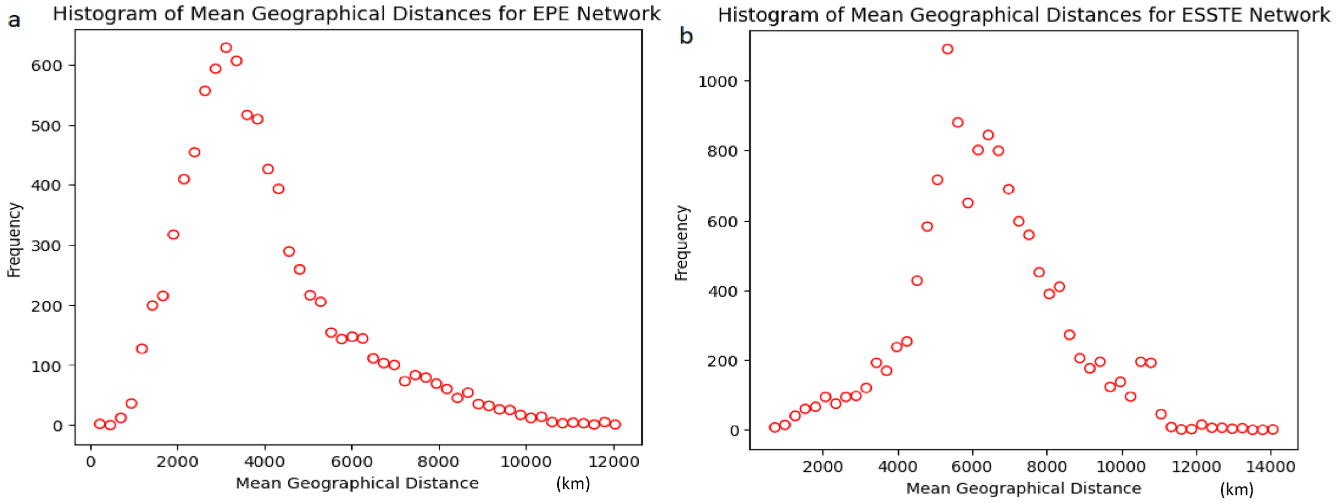

FIGURE 5 | Mean geographical distance (MGD) histogram for the (a) EPE and (b) ESSTE networks. [Colour figure can be viewed at wileyonlinelibrary.com]

June–July–August. Here, however, we did not detect any hub in such regions of the United States. This might be because our network was constructed based on monthly precipitation data and associated extreme values, while both Mondal et al. (2020) and Jamali et al. (2023) analysed daily-based data. This also means EPEs in northeastern and northern CONUS are probably synchronised at shorter time scales (daily instead of monthly).

A distinguishing feature of this study is its focus on ESSTEs rather than on general SST variability, which has been the primary emphasis of most prior studies. For example, Tantet and Dijkstra (2014) constructed a climate network from monthly SST anomalies in the HadISST dataset (1870–2011) at 2° resolution, analysing all fluctuations rather than specifically extreme events. Their network, built using Pearson correlation, covered grid points from 50°S to 80°N (6280 points) and identified hubs in the Indian Ocean (particularly South Asia), across the equatorial Pacific and along the Pacific coast of North America (see their fig. 1). Notably, in contrast to our findings, their SST-based network shows only moderate to weak hubs in several regions where we detect strong ESSTE hubs, except for East Asia, where both studies show similar patterns. These differences likely reflect both the definition of events (extremes versus monthly variability) and the distinct correlation approaches employed (linear versus nonlinear). For instance, regions characterised by frequent but moderate SST fluctuations may appear as hubs in SST-anomaly networks but not when only extreme anomalies are considered.

3.3.2 | MGD

To investigate teleconnections within the EPE and ESSTE networks and assess differences in synchronisation structures, we calculated the MGD values and analysed their histograms depicted in Figure 5.

We identified hemispheric-scale teleconnections in the ESSTE network by analysing the histogram of MGD. The histogram exhibits multiple peaks, including one around ~6000 km and a secondary peak at larger distances (approximately 10,500 km; Figure 5b), indicating the presence of long-range teleconnections connecting distant nodes. In contrast, the EPE network (Figure 5a) showed no such secondary peak, likely due to the strong spatial localisation of EPEs. This pattern supports prior observations that SST anomalies may drive regional climate variability, but do not always translate into extreme precipitation teleconnections at monthly resolution (Dittus et al. 2018; Kumar et al. 2013; Alexander et al. 2009). To study marine heatwaves at the global scale, Benedetti-Cecchi (2021) computed the distance of marine heatwaves synchronisation, analysed its distribution and found a shift from regional to large-scale patterns around 3600 km (see his fig. 5), which is shorter than 10,500 km found in this study. This is probably because Benedetti-Cecchi (2021) analysed daily SST, while we investigated monthly SST data.

We should point out that teleconnections have been previously uncovered in EPE networks at the national (Jamali et al. 2023), continental (Oladoja et al. 2025) and global (Boers et al. 2019) scales. For instance, Boers et al. (2019) identified robust global teleconnections using daily precipitation data, highlighting the critical role of high temporal resolution. In contrast, our use of monthly data facilitates long-term structural analysis but may limit the ability to capture fine-scale linkages associated with EPEs.

MGD quantifies the average physical (or geographic) distance between directly connected nodes in a network. High MGD values indicate that connected nodes in a network are, on average, far apart, meaning that the network is spatially extensive, and interactions span large areas. In Figure 6, we show the spatial variation of MGDs within the Northern Hemisphere (0°N–60°N) for both EPE and ESSTE networks using $\tau_{\max} = 0$. For the EPEs network, we found high MGD values in northwestern Mexico extending through Arizona, New Mexico and into Colorado—with isolated high values on the East Coast (North Carolina and West Virginia). Interestingly, Jamali et al. (2023), who analysed daily precipitation data and studied EPEs across CONUS, also reported high MGDs in California and Arizona during June–July–August (see their fig. 5). Consistencies between our monthly-based analyses and their daily-based ones indicate that EPEs in California and Arizona show similar synchronisation patterns across daily and monthly temporal resolutions.

We also observed regions with high MGD values extended from southern Mexico up to the entire Pacific Coast of the United States and Canada. Some high MGDs were also detected in British Columbia and throughout Manitoba in Canada. The northern part of South America also showed high MGDs, particularly in Venezuela. This pattern of high MGD values may be explained by a combination of factors: (1) monsoonal moisture transport from Mexico and the Gulf of California into the United States, (2) ARs enhancing the EPEs on the Pacific Coast, (3) mesoscale and synoptic-scale circulations from the North Tropical Atlantic and Caribbean Low-Level Jet to Venezuela (Adams and Comrie 1997; Dettinger 2011; Tim and de Bravo Guenni 2015).

For the African Sahel, we found intermediate MGDs (Figure 6). Given that this region had high *k* values (shown in Figure 4), the intermediate MGDs indicate local and regional connections. In the south of the Sahel, we found high MGDs, dominantly in Nigeria, Cameroon and Ethiopia. Schlueter et al. (2019) investigated the effect of tropical waves in northern tropical Africa and compared the impact of six wave types on precipitation during the transition and full monsoon seasons. They found that low-frequency waves (i.e., Madden–Julian Oscillation and equatorial Rossby waves) dominated the 7- to 20-day time scale and explained about up to one-third of precipitation variability. These waves are large-scale atmospheric phenomena that propagate over vast spatial domains, often spanning thousands of kilometres, and are most probably responsible for the high MGD values observed in this study.

Within Eurasia, we see high MGDs in Austria, Romania, the Caucasus (around Georgia), Kyrgyzstan, Tajikistan, East India, southeastern China and North Korea. The observed high MGDs in such regions can be attributed to several climatic and topographical factors that influence precipitation patterns over extensive areas. Within South and East Asia, long-range connections are made via the western North Pacific–North America pattern, which includes the Western Pacific Subtropical High (Ha et al. 2017). The orographic effect of the Caucasus Mountains, along with the climatological influence from the Siberian High, creates a disconnect between the precipitation experienced in the nearby countries and the source of the precipitation, as found by Forte et al. (2016). Similar phenomena have been found to influence Austria via the Alps, and precipitation shadows have been found to cause discontinuities in precipitation measurements in the Carpathian Mountains surrounding Romania (Isotta et al. 2013; Kozak et al. 2019).

The nature of MGD suggests that nodes within the darker regions are influenced by teleconnection to another non-local node and have a high likelihood of being involved in the spatially distant propagation of atmospheric conditions. Conversely, locations within the map that exhibit a lighter colouring are indicative of local influence. For the ESSTEs network, the MGD values were very high (normalised MGD > 0.8) in the areas from 0°N to 7°N and from 180°W to 150°W, from 0°N to 15°N and from 120°W to 90°W, near the equator from about 50°W to 40°W, and from 0°N to 7°N and from 140°E to 150°E (Figure 6). We also identified regions with relatively high MGDs near 30°N, extending across the Atlantic Ocean (90°W–0°W) between Central America and North Africa, and across the Pacific Ocean from approximately 120°E to 150°W. Interestingly, these regions align closely with the typical pathways of tropical cyclones, including hurricanes and typhoons. In the Atlantic, such systems often originate off the coast of West Africa, propagate westward across the ocean, and then curve northeastward towards North America. In the Pacific, they generally move westward, impacting East and Southeast Asia, and occasionally recurve northward. The alignment between these cyclone tracks and areas of elevated MGD suggests that this network-based metric is capable of capturing the dominant pathways along which large-scale atmospheric phenomena propagate.

Climatologically for ESSTEs, the low MGD values in some regions (Figure 6) imply that the ESSTEs are predominantly controlled by localised oceanic processes, such as coastal upwelling, thermocline adjustments and air–sea interactions. However, the

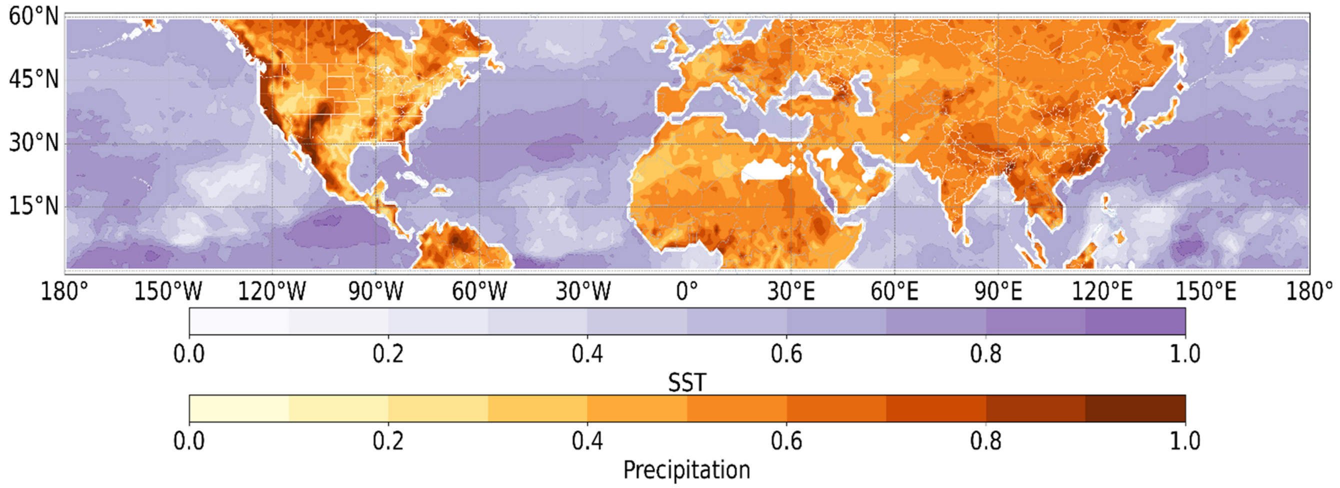

FIGURE 6 | Mean geographic distance, corrected for spatial boundary effects, within the Northern Hemisphere for the EPEs and ESSTEs from 1930 to 2020. Results for EPEs are shown with warm tones (bottom colour bar), while for ESSTEs with cool tones (top colour bar). The numerical scale is the same for both, ranging from 0 to 1. [Colour figure can be viewed at wileyonlinelibrary.com]

higher MGD exceptions indicate regions where remote climatic drivers (e.g., ENSO or the Western Pacific Warm Pool) impose long-range synchronisation patterns on the SST extremes. Overall, these MGD findings reflect the dual influence of local and distant drivers in both precipitation and SST extremes. Ocean currents play a crucial role in redistributing heat and moisture globally.

3.3.3 | Clustering Coefficient

Clustering Coefficient provides insight into how tightly knit a group of nodes is, reflecting the local cohesion within the network. A node with a high C value has strong local interconnectivity (Mondal et al. 2020). The spatial variation of the C in the Northern Hemisphere for the JJASON with $\tau_{\max} = 0$ months are shown in Figure 7 for both EPE and ESSTE networks.

Within the EPE network, North America contains mostly low to moderate C values, with small patches of high C in the Pacific Northwest, and in localised areas of western and eastern Texas, Alabama, Maryland and New Hampshire (Figure 7). The US Northwest frequently experiences ARs that make landfall and often result in heavy precipitation across coastal and mountainous terrain. This creates strong local coherence, leading to elevated clustering in climate networks. Zhang and Villarini (2018) showed that the Pacific–Japan teleconnections and the East Asian Subtropical Jet were strongly linked to the total frequency of ARs that made landfall along the western United States, a significantly stronger association than other previously examined climate modes (e.g., PDO and ENSO). In a recent study, Slinskey et al. (2023) reported that significant AR clusters frequently impact the northern Coastal Range of California and the Sierra Nevada. They found that clusters typically last for about 2 weeks, consist of four to five individual AR events per cluster and contribute to more than 85% of the total AR occurrence along the California Coastal Range.

In Africa, moderate to high C values extend from western West Africa through central Africa and into the eastern coast of Northern Africa, with specific regions (e.g., western Sahara, Niger and Chad) exhibiting very high local clustering. This pattern of high local cohesion continues to the north and east into the Middle East and Kazakhstan. Mathon et al. (2002) analysed mesoscale convective system rainfall in the Sahel and found that a subpopulation of mesoscale convective systems called organised convective systems accounted for nearly 90% of the seasonal precipitation in this region.

Climatologically, high C values in Africa suggest that strong local interactions—driven by the African Easterly Jet, surface heating and convective processes—result in closely linked precipitation patterns (Nicholson 2013; Cook 1999). In North America, moderate C values in the Pacific Northwest and the East Coast indicate that, while there is some degree of local synchronisation, these areas are less influenced by robust local processes and may instead be impacted by larger-scale phenomena. Notably, Bracken et al. (2015) observed in the Pacific Northwest that the moderate clustering reflects a balance between local convective dynamics and remote influences, such as those modulated by ENSO conditions.

In the Tropical Pacific (180°W–75°W), high C values indicate that the localised dynamics of SSTs—driven by thermocline interactions and ENSO feedback mechanisms—reinforce synchronous variability over relatively compact areas (Giannakis and Slawinska 2018). Similarly high values are found south of Greenland, south of West Africa and from western India to east of Vietnam. Similarly, regions south of Greenland and West Africa exhibit high SST clustering, reflecting localised ocean–atmosphere coupling that shapes regional climate extremes (Deser et al. 2010).

While low C values imply a reliance on broad teleconnections for synchronising extreme events, high C values are characteristic of areas where local interactions dominate the response to climatic forcing. Our findings align with the growing body of evidence from CMIP6-based studies regarding the improved coupling between SST and precipitation at monthly scales. Yang and Huang (2023) applied EOF analysis to Coupled Model Intercomparison Project Phase 6 (CMIP6) datasets and reported enhanced SST—precipitation coupling over ocean basins compared to earlier model

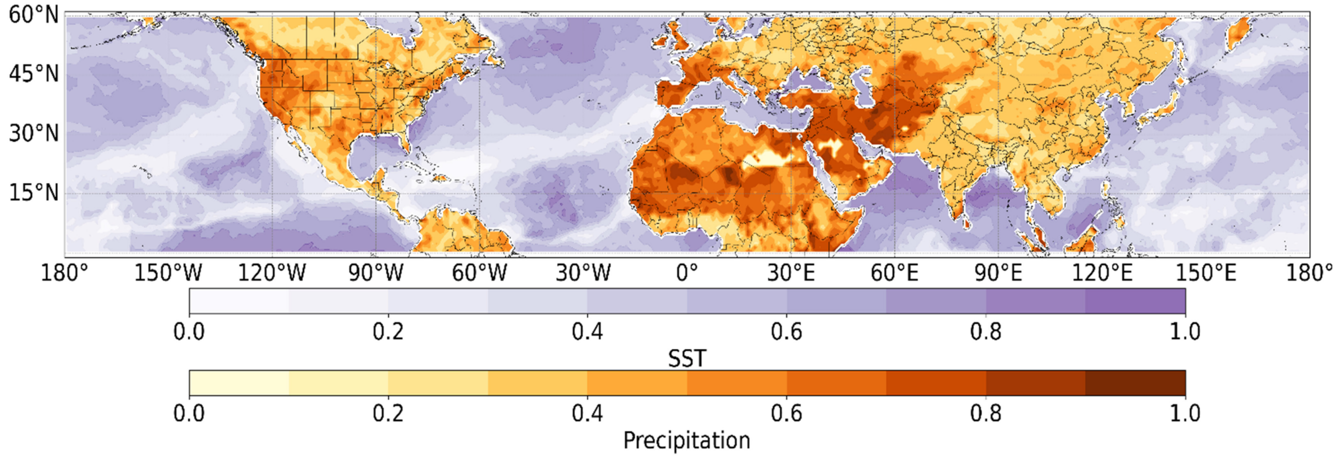

FIGURE 7 | Clustering coefficient, corrected for spatial boundary effects, within the Northern Hemisphere for the EPEs and ESSTEs from 1930 to 2020. Results for the EPEs are shown with warm tones (bottom colour bar), while for the ESSTEs with cool tones (top colour bar). The numerical scale is the same for both, ranging from 0 to 1. [Colour figure can be viewed at wileyonlinelibrary.com]

generations. Their monthly-resolution EOF framework mirrors our ESSTE network methodology, which also seeks to detect coherent SST-driven precipitation signals through spatiotemporal synchronisation. This consistency suggests that ESSTE networks not only capture known SST—precipitation coupling features but also offer a robust, network-based alternative for analysing such teleconnections.

3.4 | Connection Between EPE and ESSTE Networks

A clear connection exists between the spatial patterns of the EPE and ESSTE networks, reflecting the coupled nature of ocean–atmosphere interactions in the climate system. Although EPEs and ESSTEs were separately analysed in this study, their spatial distributions and network characteristics suggest underlying linkages mediated by large-scale climatic drivers. For instance, regions identified as ESSTE hubs in the Atlantic and Pacific Oceans (Figure 4) align with areas of high MGD (Figure 6) that correspond to major oceanic currents and pathways of tropical cyclones. These oceanic regions are well known to influence continental precipitation extremes through enhanced moisture transport, atmospheric circulation anomalies and teleconnection patterns, such as the ENSO, PDO and IOD.

The hemispheric-scale teleconnections detected in the ESSTE network (Figure 5b) indicate that extreme SST anomalies can exert far-reaching influences, potentially preconditioning atmospheric moisture and convective instability over adjacent continents where EPE hubs were found (e.g., western India, East Asia and the Sahel). Conversely, strong EPE hubs in monsoon-dominated regions (Figure 4) coincide geographically with coastal areas adjacent to warm SST extremes, suggesting that feedback mechanisms, such as latent heat release during extreme precipitation, may amplify or sustain local SST anomalies. These reciprocal interactions imply that ESSTEs can modulate the occurrence and spatial coherence of EPEs through dynamic and thermodynamic linkages, even though such cross-domain connections were not explicitly modelled in the present work.

While our current analysis treated the EPE and ESSTE networks independently, the observed spatial and teleconnection consistencies underscore the potential value of developing a *network of networks* framework in future studies. Such an approach would allow explicit quantification of inter-network linkages, identifying how nodes in the ESSTE network influence or are influenced by nodes in the EPE network through shared atmospheric pathways. Extending the synchronisation analysis to include lagged relationships and multi-layer coupling would provide deeper insight into how oceanic extremes drive terrestrial precipitation extremes, thereby advancing the predictive capability of complex network analysis for hydroclimatic extremes.

4 | Conclusion

In this study, we explored the use of complex network theory to analyse the spatiotemporal patterns of EPEs and ESSTEs from the equator to 60° N latitude in the Northern Hemisphere. Extreme values of precipitation and SST events were determined by the 95th percentile threshold at each node. The ES method was used to calculate the similarity between the extreme event series, and the EPEs and ESSTEs complex networks were constructed by setting $\tau_{\max} = 0$ months. We then calculated the network measures, that is, degree (k), MGD and clustering coefficient (C), all corrected for the spatial boundary effects. Hubs of extreme precipitation were discovered in Mexico, the African Sahel and in several locations in Asia. The MGD results for the EPEs network indicated that the following locations participated in geographically distant connections: Pacific North America, US East Coast, Venezuela, western-central and eastern Africa, Georgia, Kyrgyzstan, East India, Vietnam and southwestern China. The MGD values within the ESSTEs network were generally low, with exceptions off the southern Coast of Mexico, the eastern Coast of the French Guiana and sparsely from about 140°E to 165°E and 0°N to 15°N. Within the EPE network, spatial coherence, determined through clustering coefficient calculations, was the strongest across Africa and into the Middle East, with some moderately high to high values in the northwestern and northeastern United States and the United Kingdom. The C values obtained from the ESSTEs network were the highest in regions dominated by strong ocean–atmosphere interactions, including the Indian Ocean, East China Sea, Sea of Japan and appearing south of Mexico in a spatial pattern that contrasts with our MGD values. This relationship suggests that, while some extreme events propagate over large distances, others remain constrained by strong localised influences. These findings reinforce the ability of complex network theory to identify both regional and global synchronisation structures within climate extremes. By quantifying connectivity, spatial extent and clustering of extreme events, we demonstrated how network measures provide insight into the mechanisms governing climate variability. Our results further illustrate the contrast between terrestrial and marine extremes, where precipitation hubs are strongly tied to atmospheric circulation and orographic effects, while SST hubs align with major ocean currents and teleconnections. This distinction underscores the necessity of integrating both terrestrial and oceanic influences when modelling extreme climate events. Contrasting our results of terrestrial and marine extremes offers valuable insight for future improvements to predictive climatological models and strategies for regional adaptation.

A limitation of the present study is that the EPE and ESSTE networks were constructed and analysed independently, without explicitly quantifying the cross-network interactions between oceanic and terrestrial extremes. While this approach provides valuable insights into the internal synchronisation structures of each network, it does not capture potential feedbacks or teleconnections between extreme SST anomalies and precipitation extremes over land. Future research should therefore focus on developing a *network of networks* framework that integrates both EPE and ESSTE systems. Such an approach would enable a more comprehensive understanding of the coupled dynamics between oceanic and atmospheric extremes, shedding light on how ESSTEs may trigger, synchronise with, or modulate EPEs across regions.

Author Contributions

Connor Saari: methodology, investigation, writing – original draft, visualization, data curation, formal analysis, validation. **Jürgen Kurths:**

conceptualization, investigation, writing – original draft, validation, methodology, supervision, resources. **Gabriele Villarini:** conceptualization, investigation, writing – original draft, validation, methodology, supervision, resources. **Behzad Ghanbarian:** supervision, conceptualization, investigation, writing – original draft, validation, methodology, visualization, formal analysis, data curation, resources, project administration, writing – review and editing.

Acknowledgements

C.S. is grateful to the Geology Department, Kansas State University, for financial support through graduate teaching/research assistantships. B.G. acknowledges the University of Texas at Arlington for financial support through the faculty start-up fund and the STARs award. ChatGPT 4o was used for language editing and proofreading of this manuscript. The AI was used to improve grammar, clarity and readability. All intellectual contributions, data interpretation and conclusions remain the sole responsibility of the authors.

Conflicts of Interest

The authors declare no conflicts of interest.

Data Availability Statement

The data that support the findings of this study are available in Berkeley Earth's Global Gridded Temperature at https://berkeleyearth.org/data/. These data were derived from the following resources available in the public domain: Global Precipitation Climatology Center (GPCC), https://www.dwd.de/EN/ourservices/gpcc/gpcc.html.

References

Adam, J. C., E. A. Clark, D. P. Lettenmaier, and E. F. Wood. 2006. "Correction of Global Precipitation Products for Orographic Effects." *Journal of Climate* 19, no. 1: 15–38. https://doi.org/10.1175/jcli3604.1.

Adams, D. K., and A. C. Comrie. 1997. "The North American Monsoon." *Bulletin of the American Meteorological Society* 78, no. 10: 2197–2213. https://doi.org/10.1175/1520-0477(1997)078<2197:TNAM>2.0.CO;2.

Agarwal, A., L. Caesar, N. Marwan, R. Maheswaran, B. Merz, and J. Kurths. 2019. "Network-Based Identification and Characterization of Teleconnections on Different Scales." *Scientific Reports* 9, no. 1: 8808. https://doi.org/10.1038/s41598-019-45423-5.

Alexander, L. V. 2016. "Global Observed Long-Term Changes in Temperature and Precipitation Extremes: A Review of Progress and Limitations in IPCC Assessments and Beyond." *Weather and Climate Extremes* 11: 4–16. https://doi.org/10.1016/j.wace.2015.10.007.

Alexander, L. V., P. Uotila, and N. Nicholls. 2009. "Influence of Sea Surface Temperature Variability on Global Temperature and Precipitation Extremes." *Journal of Geophysical Research: Atmospheres* 114, no. D18: D18116.

Barros, V. R., and G. E. Silvestri. 2002. "The Relation Between Sea Surface Temperature at the Subtropical South-Central Pacific and Precipitation in Southeastern South America." *Journal of Climate* 15, no. 3: 251–267. https://doi.org/10.1175/1520-0442(2002)015<0251:TRBSST>2.0.CO;2.

Benedetti-Cecchi, L. 2021. "Complex Networks of Marine Heatwaves Reveal Abrupt Transitions in the Global Ocean." *Scientific Reports* 11, no. 1: 1739. https://doi.org/10.1038/s41598-021-81369-3.

Boers, N., B. Bookhagen, N. Marwan, J. Kurths, and J. Marengo. 2013. "Complex Networks Identify Spatial Patterns of Extreme Rainfall Events of the South American Monsoon System." *Geophysical Research Letters* 40, no. 16: 4386–4392.

Boers, N., B. Goswami, A. Rheinwalt, B. Bookhagen, B. Hoskins, and J. Kurths. 2019. "Complex Networks Reveal Global Pattern of Extreme-Rainfall Teleconnections." *Nature* 566, no. 7744: 373–377. https://doi.org/10.1038/s41586-018-0872-x.

Boers, N., B. Bookhagen, H. M. Barbosa, N. Marwan, J. Kurths, and J. A. Marengo. 2014. "Prediction of Extreme Floods in the Eastern Central Andes Based on a Complex Networks Approach." *Nature Communications* 5, no. 1: 5199.

Bosikun, K., T. Jamali, B. Ghanbarian, and J. Kurths. 2025. "Complex Network Analysis of Extreme Temperature Events in the Contiguous United States." *Atmospheric Research* 318: 107995. https://doi.org/10.1016/j.atmosres.2025.107995.

Bothe, O., K. Fraedrich, and X. Zhu. 2011. "Precipitation Climate of Central Asia and the Large-Scale Atmospheric Circulation." *Theoretical and Applied Climatology* 108, no. 3–4: 345–354. https://doi.org/10.1007/s00704-011-0537-2.

Bracken, C., B. Rajagopalan, M. Alexander, and S. Gangopadhyay. 2015. "Spatial Variability of Seasonal Extreme Precipitation in the Western United States." *Journal of Geophysical Research: Atmospheres* 120, no. 10: 4522–4533. https://doi.org/10.1002/2015jd023205.

Buishand, T. A. 1989. "Statistics of Extremes in Climatology." *Statistica Neerlandica* 43, no. 1: 1–30. https://doi.org/10.1111/j.1467-9574.1989.tb01244.x.

Cook, K. H. 1999. "Generation of the African Easterly Jet and Its Role in Determining West African Precipitation." *Journal of Climate* 12, no. 5: 1165–1184. https://doi.org/10.1175/1520-0442(1999)012<>2.0.co;2.

Copernicus Climate Change Service. 2023. "Record-Breaking North Atlantic Ocean Temperatures Contribute to Extreme Marine Heatwaves." Accessed June 25, 2025. https://climate.copernicus.eu/record-breaking-north-atlantic-ocean-temperatures-contribute-extreme-marine-heatwaves.

Cui, D., C. Wang, and J. Santisirisomboon. 2019. "Characteristics of Extreme Precipitation Over Eastern Asia and Its Possible Connections With Asian Summer Monsoon Activity." *International Journal of Climatology* 39: 711–723.

Dare, R. A., and J. L. McBride. 2011. "The Threshold Sea Surface Temperature Condition for Tropical Cyclogenesis." *Journal of Climate* 24, no. 17: 4570–4576. https://doi.org/10.1175/jcli-d-10-05006.1.

Deser, C., M. A. Alexander, S. P. Xie, and A. S. Phillips. 2010. "Sea Surface Temperature Variability: Patterns and Mechanisms." *Annual Review of Marine Science* 2, no. 1: 115–143. https://doi.org/10.1146/annurev-marine-120408-151453.

Dettinger, M. 2011. "Climate Change, Atmospheric Rivers, and Floods in California—A Multimodel Analysis of Storm Frequency and Magnitude Changes." *JAWRA Journal of the American Water Resources Association* 47, no. 3: 514–523. https://doi.org/10.1111/j.1752-1688.2011.00546.x.

Dittus, A. J., D. J. Karoly, M. G. Donat, S. C. Lewis, and L. V. Alexander. 2018. "Understanding the Role of Sea Surface Temperature-Forcing for Variability in Global Temperature and Precipitation Extremes." *Weather and Climate Extremes* 21: 1–9. https://doi.org/10.1016/j.wace.2018.06.002.

Dong, L., L. R. Leung, F. Song, and J. Lu. 2018. "Roles of SST Versus Internal Atmospheric Variability in Winter Extreme Precipitation Variability Along the U.S. West Coast." *Journal of Climate* 31, no. 19: 8039–8058. https://doi.org/10.1175/jcli-d-18-0062.1.

Donges, J. F., Y. Zou, N. Marwan, and J. Kurths. 2009. "Complex Networks in Climate Dynamics." *European Physical Journal Special Topics* 174, no. 1: 157–179. https://doi.org/10.1140/epjst/e2009-01098-2.

Ekhtiari, N., A. Agarwal, N. Marwan, and R. V. Donner. 2019. "Disentangling the Multi-Scale Effects of Sea-Surface Temperatures on Global Precipitation: A Coupled Networks Approach." *Chaos (Woodbury, N.Y.)* 29, no. 6: 063116. https://doi.org/10.1063/1.5095565.

Ekhtiari, N., C. Ciemer, C. Kirsch, and R. V. Donner. 2021. "Coupled Network Analysis Revealing Global Monthly Scale Co-Variability Patterns Between Sea-Surface Temperatures and Precipitation in Dependence on the Enso State." *European Physical Journal Special Topics* 230, no. 14–15: 3019–3032. https://doi.org/10.1140/epjs/s11734-021-00168-z.

Falga, R., and C. Wang. 2022. "The Rise of Indian Summer Monsoon Precipitation Extremes and Its Correlation With Long-Term Changes of Climate and Anthropogenic Factors." *Scientific Reports* 12, no. 1: 11985. https://doi.org/10.1038/s41598-022-16240-0.

Fan, J., J. Meng, J. Ludescher, et al. 2021. "Statistical Physics Approaches to the Complex Earth System." *Physics Reports* 896: 1–84. https://doi.org/10.1016/j.physrep.2020.09.005.

Feldhoff, J., J. H. Feldhoff, S. Lange, et al. 2014. "Complex Networks for Climate Model Evaluation With Application to Statistical Versus Dynamical Modeling of South American Climate." *Climate Dynamics* 44, no. 5–6: 1567–1581. https://doi.org/10.1007/s00382-014-2182-9.

Forte, A. M., K. X. Whipple, B. Bookhagen, and M. W. Rossi. 2016. "Decoupling of Modern Shortening Rates, Climate, and Topography in the Caucasus." *Earth and Planetary Science Letters* 449: 282–294. https://doi.org/10.1016/j.epsl.2016.06.013.

Fowler, H. J., G. Lenderink, A. F. Prein, et al. 2021. "Anthropogenic Intensification of Short-Duration Rainfall Extremes." *Nature Reviews Earth and Environment* 2, no. 2: 107–122. https://doi.org/10.1038/s43017-020-00128-6.

Garner, A. J., R. E. Kopp, and B. P. Horton. 2021. "Evolving Tropical Cyclone Tracks in the North Atlantic in a Warming Climate." *Earth's Future* 9, no. 12: e2021EF002326.

Giannakis, D., and J. Slawinska. 2018. "Indo-Pacific Variability on Seasonal to Multidecadal Time Scales. Part II: Multiscale Atmosphere–Ocean Linkages." *Journal of Climate* 31, no. 2: 693–725. https://doi.org/10.1175/jcli-d-17-0031.1.

Green, J., I. D. Haigh, N. Quinn, et al. 2025. "Review Article: A Comprehensive Review of Compound Flooding Literature With a Focus on Coastal and Estuarine Regions." *Natural Hazards and Earth System Sciences* 25, no. 2: 747–816. https://doi.org/10.5194/nhess-25-747-2025.

Groisman, P. Y., R. W. Knight, D. R. Easterling, T. R. Karl, G. C. Hegerl, and V. N. Razuvaev. 2005. "Trends in Intense Precipitation in the Climate Record." *Journal of Climate* 18, no. 9: 1326–1350. https://doi.org/10.1175/jcli3339.1.

Gupta, S., Z. Su, N. Boers, J. Kurths, N. Marwan, and F. Pappenberger. 2022. "Interconnection Between the Indian and the East Asian Summer Monsoon: Spatial Synchronization Patterns of Extreme Rainfall Events." *International Journal of Climatology* 43, no. 2: 1034–1049. https://doi.org/10.1002/joc.7861.

Ha, K.-J., Y.-W. Seo, J.-Y. Lee, R. H. Kripalani, and K.-S. Yun. 2017. "Linkages Between the South and East Asian Summer Monsoons: A Review and Revisit." *Climate Dynamics* 51, no. 11–12: 4207–4227. https://doi.org/10.1007/s00382-017-3773-z.

Hannachi, A., S. Unkel, N. T. Trendafilov, and I. T. Jolliffe. 2009. "Independent Component Analysis of Climate Data: A New Look at EOF Rotation." *Journal of Climate* 22, no. 11: 2797–2812. https://doi.org/10.1175/2008jcli2571.1.

Hatsuzuka, D., and T. Sato. 2022. "Impact of SST on Present and Future Extreme Precipitation in Hokkaido Investigated Considering Weather Patterns." *Journal of Geophysical Research: Atmospheres* 127: e2021JD036120. https://doi.org/10.1029/2021JD036120.

He, J., N. C. Johnson, G. A. Vecchi, B. Kirtman, A. T. Wittenberg, and S. Sturm. 2018. "Precipitation Sensitivity to Local Variations in Tropical Sea Surface Temperature." *Journal of Climate* 31, no. 22: 9225–9238. https://doi.org/10.1175/jcli-d-18-0262.1.

Intergovernmental Panel on Climate Change (IPCC). 2023. "Climate Change 2021—The Physical Science Basis [Preprint]." https://doi.org/10.1017/9781009157896.

Isotta, F. A., C. Frei, V. Weilguni, et al. 2013. "The Climate of Daily Precipitation in the Alps: Development and Analysis of a High-Resolution Grid Dataset From Pan-Alpine Rain-Gauge Data." *International Journal of Climatology* 34, no. 5: 1657–1675. https://doi.org/10.1002/joc.3794.

Jamali, T., B. Ghanbarian, and J. Kurths. 2023. "Spatiotemporal Analysis of Extreme Precipitation Events in the United States at Mesoscale: Complex Network Theory." *Journal of Hydrology* 627: 130440. https://doi.org/10.1016/j.jhydrol.2023.130440.

Kane, R. P. 1999. "El Niño Timings and Rainfall Extremes in India, Southeast Asia and China." *International Journal of Climatology* 19: 653–672.

Kang, Y., J. H. Jeong, and D. I. Lee. 2021. "Influence of Sea Surface Temperature on a Mesoscale Convective System Producing Extreme Rainfall Over the Yellow Sea." *Monthly Weather Review* 149, no. 8: 2613–2632.

Knutson, T., S. J. Camargo, J. C. L. Chan, et al. 2020. "Tropical Cyclones and Climate Change Assessment: Part II: Projected Response to Anthropogenic Warming." *Bulletin of the American Meteorological Society* 101, no. 3: E303–E322. https://doi.org/10.1175/bams-d-18-0194.1.

Kotz, M., A. Levermann, and L. Wenz. 2022. "The Effect of Rainfall Changes on Economic Production." *Nature* 601, no. 7892: 223–227. https://doi.org/10.1038/s41586-021-04283-8.

Kozak, J., D. Cebulak, T. Stec, and A. Jaguś. 2019. "Variation of Precipitation Gradient in Mountain Areas Based on the Example of the Western Beskids in the Polish Carpathians." *Journal of Ecological Engineering* 20, no. 9: 261–266. https://doi.org/10.12911/22998993/112502.

Kumar, A., L. Zhang, and W. Wang. 2013. "Sea Surface Temperature–Precipitation Relationship in Different Reanalyses." *Monthly Weather Review* 141, no. 3: 1118–1123. https://doi.org/10.1175/mwr-d-12-00214.1.

Kunze, S. 2021. "Unraveling the Effects of Tropical Cyclones on Economic Sectors Worldwide: Direct and Indirect Impacts." *Environmental and Resource Economics* 78, no. 4: 545–569. https://doi.org/10.1007/s10640-021-00541-5.

Lindsey, R., and L. Dahlman. 2025. "Climate Change: Global Temperature." *Climate. Gov* 16: 1–5. https://www.climate.gov/news-features/understanding-climate/climate-change-global-temperature.

Ludescher, J., M. Martin, N. Boers, et al. 2021. "Network-Based Forecasting of Climate Phenomena." *Proceedings of the National Academy of Sciences* 118, no. 47: e1922872118.

Malik, N., N. Marwan, and J. Kurths. 2010. "Spatial Structures and Directionalities in Monsoonal Precipitation Over South Asia." *Nonlinear Processes in Geophysics* 17, no. 5: 371–381.

Marvel, K., and C. Bonfils. 2013. "Identifying External Influences on Global Precipitation." *Proceedings of the National Academy of Sciences of the United States of America* 110, no. 48: 19301–19306. https://doi.org/10.1073/pnas.1314382110.

Mathon, V., H. Laurent, and T. Lebel. 2002. "Mesoscale Convective System Rainfall in the Sahel." *Journal of Applied Meteorology* 41, no. 11: 1081–1092. https://doi.org/10.1175/1520-0450(2002)041<1081:MCSRIT>2.0.CO;2.

Merchant, C. J., R. P. Allan, and O. Embury. 2025. "Quantifying the Acceleration of Multidecadal Global Sea Surface Warming Driven by Earth's Energy Imbalance." *Environmental Research Letters* 20, no. 2: 024037. https://doi.org/10.1088/1748-9326/adaa8a.

Mondal, S., A. K. Mishra, and L. R. Leung. 2020. "Spatiotemporal Characteristics and Propagation of Summer Extreme Precipitation Events Over United States: A Complex Network Analysis." *Geophysical Research Letters* 47: e2020GL088185. https://doi.org/10.1029/2020GL088185.

Mullens, E. D. 2021. "Meteorological Cause and Characteristics of Widespread Heavy Precipitation in the Texas Gulf Watershed 2003–2018." *International Journal of Climatology* 41, no. 6: 3743–3760.

Murgulet, D., M. Valeriu, R. R. Hay, P. Tissot, and A. M. Mestas-Nuñez. 2017. "Relationships Between Sea Surface Temperature Anomalies in the Pacific and Atlantic Oceans and South Texas Precipitation and Streamflow Variability." *Journal of Hydrology* 550: 726–739. https://doi.org/10.1016/j.jhydrol.2017.05.041.

Nicholson, S. E. 2013. "The West African Sahel: A Review of Recent Studies on the Rainfall Regime and Its Interannual Variability." *ISRN Meteorology* 2013: 1–32. https://doi.org/10.1155/2013/453521.

Novi, L., A. Bracco, and F. Falasca. 2021. "Uncovering Marine Connectivity Through Sea Surface Temperature." *Scientific Reports* 11, no. 1: 8839. https://doi.org/10.1038/s41598-021-87711-z.

O'Gorman, P. A. 2015. "Precipitation Extremes Under Climate Change." *Current Climate Change Reports* 1, no. 2: 49–59. https://doi.org/10.1007/s40641-015-0009-3.

Oladoja, V., T. Jamali, B. Ghanbarian, and J. Kurths. 2025. "Analyzing Spatiotemporal Patterns of Extreme Precipitations in North America Using Complex Network Theory." *Journal of Hydrology* 661: 133492. https://doi.org/10.1016/j.jhydrol.2025.133492.

Paprotny, D., A. Sebastian, O. Morales-Nápoles, and S. N. Jonkman. 2018. "Trends in Flood Losses in Europe Over the Past 150 Years." *Nature Communications* 9, no. 1: 1985. https://doi.org/10.1038/s41467-018-04253-1.

Quiroga, R. Q., T. Kreuz, and P. Grassberger. 2002. "Event Synchronization: A Simple and Fast Method to Measure Synchronicity and Time Delay Patterns." *Physical Review E* 66, no. 4: 041904. https://doi.org/10.1103/physreve.66.041904.

Rheinwalt, A., N. Marwan, J. Kurths, P. Werner, and F. W. Gerstengarbe. 2012. "Boundary Effects in Network Measures of Spatially Embedded Networks." *Europhysics Letters* 100, no. 2: 28002. https://doi.org/10.1209/0295-5075/100/28002.

Roxy, M. 2013. "Sensitivity of Precipitation to Sea Surface Temperature Over the Tropical Summer Monsoon Region—And Its Quantification." *Climate Dynamics* 43, no. 5–6: 1159–1169. https://doi.org/10.1007/s00382-013-1881-y.

Rummukainen, M. 2012. "Changes in Climate and Weather Extremes in the 21st Century." *WIREs Climate Change* 3, no. 2: 115–129. https://doi.org/10.1002/wcc.160.

Scarsoglio, S., F. Laio, and L. Ridolfi. 2013. "Climate Dynamics: A Network-Based Approach for the Analysis of Global Precipitation." *PLoS One* 8, no. 8: e71129. https://doi.org/10.1371/journal.pone.0071129.

Schlueter, A., A. H. Fink, P. Knippertz, and P. Vogel. 2019. "A Systematic Comparison of Tropical Waves Over Northern Africa. Part I: Influence on Rainfall." *Journal of Climate* 32, no. 5: 1501–1523. https://doi.org/10.1175/jcli-d-18-0173.1.

Shehzad, K. 2023. "Extreme Flood in Pakistan: Is Pakistan Paying the Cost of Climate Change? A Short Communication." *Science of the Total Environment* 880: 162973. https://doi.org/10.1016/j.scitotenv.2023.162973.

Shige, S., and C. D. Kummerow. 2016. "Precipitation-Top Heights of Heavy Orographic Rainfall in the Asian Monsoon Region." *Journal of the Atmospheric Sciences* 73, no. 8: 3009–3024. https://doi.org/10.1175/jas-d-15-0271.1.

Singh, O. P. 2001. "Cause-Effect Relationships Between Sea Surface Temperature, Precipitation and Sea Level Along the Bangladesh Coast." *Theoretical and Applied Climatology* 68, no. 3–4: 233–243. https://doi.org/10.1007/s007040170048.

Slinskey, E. A., A. Hall, N. Goldenson, P. C. Loikith, and J. Norris. 2023. "Subseasonal Clustering of Atmospheric Rivers Over the Western United States." *Journal of Geophysical Research: Atmospheres* 128: e2023JD038833. https://doi.org/10.1029/2023JD038833.

Strnad, F. M., K. M. Hunt, N. Boers, and B. Goswami. 2025. "Intraseasonal Synchronization of Extreme Rainfall Between North India and the Sahel." *Quarterly Journal of the Royal Meteorological Society* 151: e4946.

Sun, H., and D. J. Furbish. 1997. "Annual Precipitation and River Discharges in Florida in Response to El Niño- and La Niña-Sea Surface Temperature Anomalies." *Journal of Hydrology* 199, no. 1–2: 74–87. https://doi.org/10.1016/s0022-1694(96)03303-3.

Tantet, A., and H. A. Dijkstra. 2014. "An Interaction Network Perspective on the Relation Between Patterns of Sea Surface Temperature Variability and Global Mean Surface Temperature." *Earth System Dynamics* 5, no. 1: 1–14. https://doi.org/10.5194/esd-5-1-2014.

Terry, J. P., and I. H. Kim. 2015. "Morphometric Analysis of Tropical Storm and Hurricane Tracks in the North Atlantic Basin Using a Sinuosity-Based Approach." *International Journal of Climatology* 35, no. 5: 923–934.

Thompson, D. W., J. M. Wallace, J. J. Kennedy, and P. D. Jones. 2010. "An Abrupt Drop in Northern Hemisphere Sea Surface Temperature Around 1970." *Nature* 467, no. 7314: 444–447. https://doi.org/10.1038/nature09394.

Tim, N., and L. de Bravo Guenni. 2015. "Oceanic Influence on the Precipitation in Venezuela Under Current and Future Climate." *Climate Dynamics* 47: 211–234. https://doi.org/10.1007/s00382-015-2832-6.

Ting, M., and H. Wang. 1997. "Summertime U.S. Precipitation Variability and Its Relation to Pacific Sea Surface Temperature." *Journal of Climate* 10, no. 8: 1853–1873. https://doi.org/10.1175/1520-0442(1997)010<1853:SUSPVA>2.0.CO;2.

Trenberth, K. 2011. "Changes in Precipitation With Climate Change." *Climate Research* 47, no. 1: 123–138. https://doi.org/10.3354/cr00953.

Trenberth, K. E., and D. J. Shea. 2005. "Relationships Between Precipitation and Surface Temperature." *Geophysical Research Letters* 32, no. 14: L14703.

van der Ent, R. J., and H. H. Savenije. 2013. "Oceanic Sources of Continental Precipitation and the Correlation With Sea Surface Temperature." *Water Resources Research* 49, no. 7: 3993–4004. https://doi.org/10.1002/wrcr.20296.

Walsh, K. J. E., J. L. McBride, P. J. Klotzbach, et al. 2015. "Tropical Cyclones and Climate Change." *WIREs Climate Change* 7, no. 1: 65–89. https://doi.org/10.1002/wcc.371.

Wang, J., X. Guan, and S. Miao. 2025. "Spatiotemporal Evolution Patterns of Flood-Causing Rainstorm Events in China From a 3D Perspective." *Atmospheric Research* 315: 107920. https://doi.org/10.1016/j.atmosres.2025.107920.

Yang, X., and P. Huang. 2023. "Improvements in the Relationship Between Tropical Precipitation and Sea Surface Temperature From CMIP5 to CMIP6." *Climate Dynamics* 60, no. 11: 3319–3337.

Zhang, M., H. Yu, A. D. King, Y. Wei, J. Huang, and Y. Ren. 2020. "Greater Probability of Extreme Precipitation Under 1.5°C and 2°C Warming Limits Over East-Central Asia." *Climatic Change* 162, no. 2: 603–619. https://doi.org/10.1007/s10584-020-02725-2.

Zhang, W., and G. Villarini. 2018. "Uncovering the Role of the East Asian Jet Stream and Heterogeneities in Atmospheric Rivers Affecting the Western United States." *Proceedings of the National Academy of Sciences of the United States of America* 115, no. 5: 891–896. https://doi.org/10.1073/pnas.1717883115.

Zhao, D., X. Yang, W. Song, W. Zhang, and D. Huang. 2023. "Visibility Graph Analysis of the Sea Surface Temperature Irreversibility During El Niño Events." *Nonlinear Dynamics* 111, no. 18: 17393–17409. https://doi.org/10.1007/s11071-023-08762-7.

Zittis, G., M. Almazroui, P. Alpert, et al. 2022. "Climate Change and Weather Extremes in the Eastern Mediterranean and Middle East." *Reviews of Geophysics* 60: e2021RG000762. https://doi.org/10.1029/2021RG000762.

Appendix A

Explanation of White Nodes in MGD and Clustering Coefficient Maps

In Figures 6 and 7, certain nodes located in Africa, Saudi Arabia and Afghanistan appear as white areas in the MGD and clustering coefficient maps. To investigate this, we conducted additional analyses and found that these nodes exhibit zero event synchronisation (ES) values in the ES matrix (Figure A1), indicating no significant links to any other nodes. Correspondingly, these nodes also have zero *k* values in the degree centrality map (Figure 4). Since both MGD and *C* are mathematically dependent on node degree, as described in Equations (4) and (5), a zero degree results in undefined (NaN) values for these metrics (Figure A2). Consequently, the affected nodes are rendered as white in the corresponding visualisations.

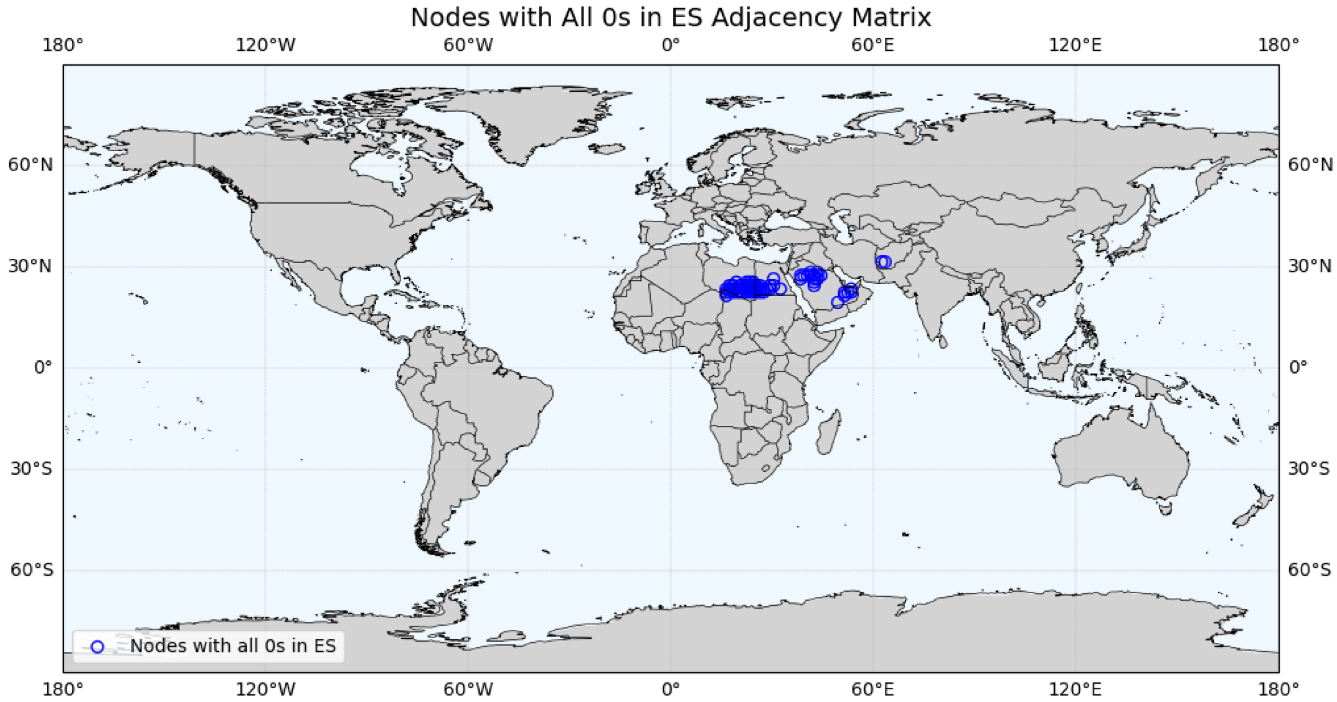

FIGURE A1 | Nodes with zero values in the ES matrix in the Northern Hemisphere. [Colour figure can be viewed at wileyonlinelibrary.com]

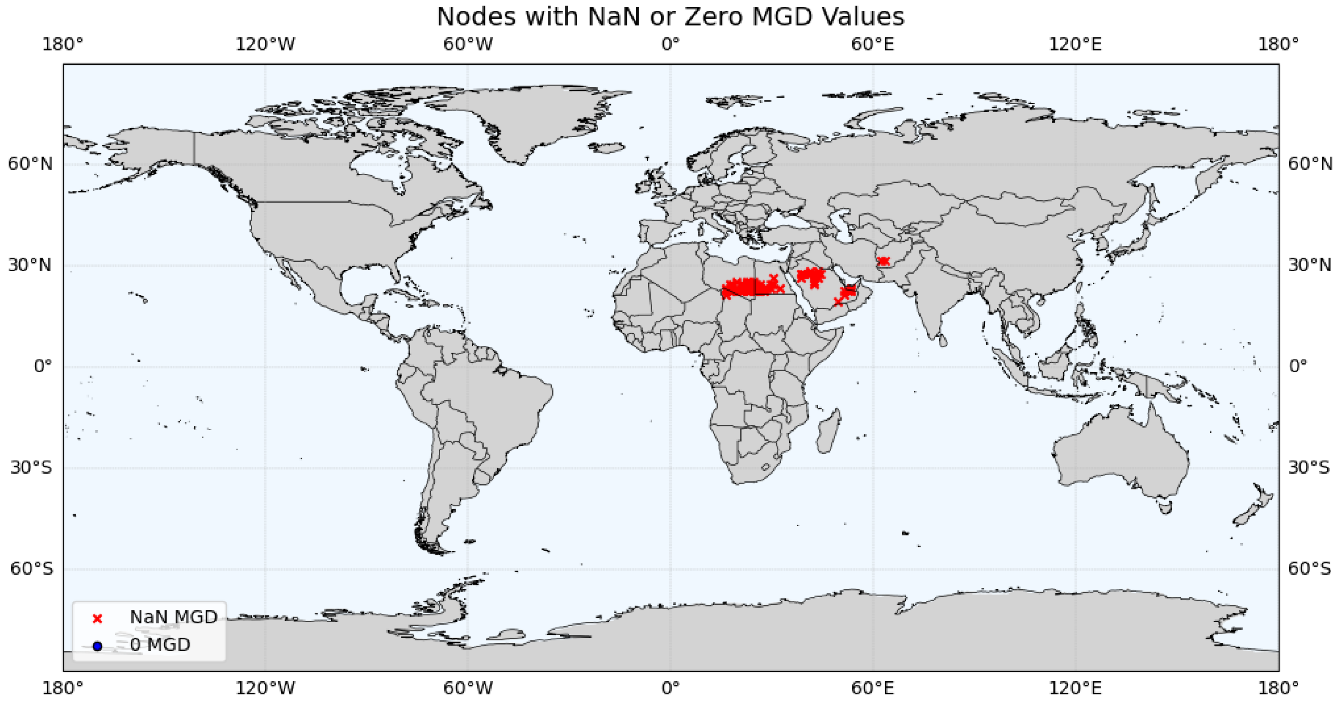

FIGURE A2 | Nodes with either NAN or zero MGD values in the Northern Hemisphere. [Colour figure can be viewed at wileyonlinelibrary.com]